A Soft, Lightweight Flipping Robot With Versatile Motion Capabilities for Wall-Climbing Applications

Rui Chen, *Member, IEEE*, Xinrui Tao, Changyong Cao, *Member, IEEE*, Pei Jiang, *Member, IEEE*, Jun Luo, and Yu Sun, *Fellow, IEEE*

***Abstract*—Soft wall-climbing robots have been limited in their ability to perform complex locomotion in diverse environments due to their structure and weight. Thus far, soft wall-climbing robots with integrated functions that can locomote in complex 3-D environments are yet to be developed. This article addresses this challenge by presenting a lightweight (2.57 g) soft wall-climbing robot with integrated linear, turning, and transitioning motion capabilities. The soft robot employs three pneumatic bending actuators and two adaptive electroadhesion pads, which enable it to flip forward, transition between two walls, turn in two directions, and adhere to various surfaces. Different motion and control strategies are proposed based on a theoretical model. The experimental results demonstrate that the robot can move at an average speed of 3.85 mm/s (0.08 body length/s) on horizontal, vertical, and inverted walls and make transitions between walls with different pinch angles within 180°. Additionally, the soft robot can carry a miniature camera on vertical walls to perform detection and surveillance tasks. This article provides a reliable structure and control strategy to enhance the multifunctionality of soft wall-climbing robots and enable their applications in unstructured environments.**

***Index Terms*—Electroadhesion (EA), flipping locomotion, soft climbing robot, versatile motions.**

I. Introduction

WALL-CLIMBING robots have progressed rapidly over the past few decades, finding applications in cleaning, inspection, maintenance, and monitoring [1], [2], [3]. However, these robots often rely on rigid structures, such as wheels [4], [5], tracks [6], feet [7], [8], and propellers [9], which have limited ability and poor stability in rugged terrains and are complex to control [10]. The emergence of soft robots has opened new possibilities for wall-climbing robots. Compared with traditional rigid robots, soft robots made of soft materials offer infinite degrees of freedom, high adaptability and flexibility, and safe human–robot interactions. Additionally, their simple structure allows for more straightforward manufacturing and control [11], [12].

For soft wall-climbing robots, climbing performance mainly depends on the development of actuators and adhesion methods. Pneumatic actuators are widely used due to their simplicity and significant deformation [13], [14], [15], [16], [17]. Shape memory alloy (SMA) [18], [19], [20] and dielectric elastomer (DE) actuators [21], [22], [23] are also popular owing to their lightness and easy operation. Vacuum adsorption is a good choice for soft wall-climbing robots that require a strong adsorption force [24], [25]. Electroadhesion (EA), with its simple structure and good surface adaptation [26], is more attractive for miniaturized and lightweight robots [20], [22].

In addition to actuation and adhesion, the control strategies also have a significant impact on performance. High-frequency control voltages are widely used in soft robots with small deformation actuators (e.g., DE-actuated robots [21], [22], [23]) to quickly switch the deformation of the actuators and the adhesion state of the foot to achieve inchworm-type motion. However, this control method is only suitable for simple, repetitive movements. For pneumatically actuated soft robots, large deformations can be achieved by controlling the pressure of the actuators through air pumps and valves. It is also possible to use theoretical models or sensors to make the pumps and valves operate in an intelligent way [27], [28], enabling the robot to perform adjustable inchworm-type [29] or flip motion [30] to cope with various situations.

Moreover, soft wall-climbing robots have evolved beyond their single climbing function to develop multiple motion capabilities to meet the demands of working in unstructured environments, building on the aforementioned actuation and control methods [14], [31]. Some desired motion capabilities, such as turning, can expand a robot's workspace from a straight line to a 2-D plane. For example, Gu et al. [32] developed a wall-climbing robot that can turn by connecting two individual units and moving them at different speeds. Qin et al. [33]

Manuscript received 28 February 2023; revised 8 May 2023; accepted 15 June 2023. This work was supported in part by the National Key Research and Development Project of China under Grant 2020YFB1313000, in part by the National Natural Science Foundation of China under Grant 52075051, in part by the Natural Science Foundation of Chongqing, China under Grant cstc2021jcyj-msxmX0908, and in part by the Fundamental Research Funds for the Central Universities under Grant 2021CDJQY-015. This paper was recommended for publication by Associate Editor Y. Sun and Editor A. Menciassi upon evaluation of the reviewers' comments. *(Corresponding author: Rui Chen.)*

Rui Chen, Xinrui Tao, Pei Jiang, and Jun Luo are with the State Key Laboratory of Mechanical Transmissions, Chongqing University, Chongqing 400044, China. (e-mail: cr@cqu.edu.cn; 202007021104t@cqu.edu.cn; peijiang@cqu.edu.cn; luoj@cqu.edu.cn).

Changyong Cao is with the Department of Mechanical and Aerospace Engineering, Case Western Reserve University, Cleveland, OH 44106 USA, and with the Department of Electrical, Computer, and Systems Engineering, Case Western Reserve University, Cleveland, OH 44106 USA, and also with the Advanced Platform Technology Center, Louis Stokes Cleveland VA Medical Center, Cleveland, OH 44106 USA. (e-mail: ccao@case.edu).

Yu Sun is with the Advanced Micro and Nanosystems Laboratory, University of Toronto, Toronto, ON M5S 3G8, Canada. (e-mail: sun@mie.utoronto.ca).

This article has supplementary material provided by the authors and color versions of one or more figures available at https://doi.org/10.1109/TRO.2023.3294920.

Digital Object Identifier 10.1109/TRO.2023.3294920

TABLE I
COMPARISON OF THE PERFORMANCE AND CAPABILITIES OF DIFFERENT SOFT CLIMBING ROBOTS

Soft wall-climbing robot	Actuation method	Self-weight (g)	Wall climbing	Climbing speed (BL/s)	Single-body turning	Transition	Curved surface
G. Gu *et al*. [32]	Dielectric elastomer	2	Vertical	0.75	No	No	No
Y. Guo *et al.* [35]	Dielectric elastomer	12	Vertical	0.021	Yes	No	No
W. Pang *et al*. [36]	LCE actuation	3	Vertical/inverted	0.018	No	Yes	Yes
Y. Tang *et al*. [25]	Pneumatic	40	Vertical	0.026	No	No	No
L. Qin *et al*. [33]	Pneumatic	43	Vertical	0.049	Yes	No	No
H. Fu *et al*. [30]	Pneumatic	25	Vertical	0.062	No	Yes	No
Y. Zhang *et al*. [29]	Pneumatic	33.33	Vertical	0.079	No	Yes	No
B. Liao *et al*. [34]	Pneumatic	20	Only on rods	0.193	Yes	No	Yes
M. S. Verma *et al*. [37]	Pneumatic	98	Only in tubes	0.072	Yes	No	Yes
This work	**Pneumatic**	**2.57**	**Vertical/inverted**	**0.08**	**Yes**	**Yes**	**Yes**

BL, body length; LCE, liquid crystal elastomer.

demonstrated efficient and fast turning motion in their versatile soft crawling robot using two parallel pneumatic actuators.

In addition to moving along a single plane, soft robots face a significant challenge in achieving transitioning motions between walls. The ability to make transitions between different walls can extend the soft robots' workspace, enabling them to move freely in 3-D environments. Fu et al. [30] designed soft robots with two suction cups and a two-segment reinforced actuator that can lift its own weight and transition to a vertical wall. Inspired by the multimodal locomotion capability of inchworms, Zhang et al. [29] developed a soft crawling-climbing robot with three pneumatic artificial muscles. To transition from crawling to climbing, artificial muscles lifted the front feet from the ground to the vertical wall. Additionally, soft robots have been developed to move on curved surfaces, such as pipes [31] or rods [34] for expanding the workspace.

While existing soft climbing robots have various functions, such as turning, transitioning, and climbing on curved surfaces, integrating these functions into a single soft robot is still challenging, as shown in Table I. The difficulty in solving this problem mainly lies in climbing stability and structural simplification. Multiple motion functions require more actuators and significant deformations, increasing the risk of the soft robot falling off the wall. Therefore, it is essential to design a lightweight structure and a stable adsorption method to cope with various wall environments and the peeling force caused by multiple motions. Different functions also require different motions for implementation. For example, turning requires a motion to change the angle of the front and rear foot, and transition requires motions to lift the body and adjust the angle of the foot. A suitable structure that is compatible with all functional requirements without being complicated is necessary to make the robot reliable and easy to control.

In this article, we developed a lightweight and versatile soft wall-climbing robot with a simple structure consisting of three actuators. The soft robot can perform versatile motion capabilities, such as turning in two directions, transitioning between two walls, moving on vertical and inverted walls, and climbing on curved surfaces via flipping locomotion. We also designed an adaptive footpad to achieve stable adhesion and surface adaptability. Furthermore, we proposed a control strategy based on a theoretical model for real-time control of the soft robot under different conditions. The entire soft robot only weighs 2.57 g. Our experiments showed that the soft robot could move linearly on horizontal walls with an average speed of 3.85 mm/s. Interestingly, it can also move on vertical and inverted walls without compromising its speed due to its light self-weight. The robot can turn in either clockwise or counterclockwise directions at an average speed of 2.23°/s and 2.97°/s, respectively. In addition, the robot can carry a 1.2 g miniature camera to complete the horizontal-to-vertical transition and climb on a vertical wall for surveillance tasks.

This article presents two main novelties and contributions:

1) A novel and versatile structure for soft wall-climbing robots that can adapt to multiple wall environments using flipping locomotion. The structure provides a design concept for integrating multiple functionalities into a reliable and straightforward soft wall-climbing robot.
2) A new pneumatic control method based on theoretical models for soft robots. By establishing a numerical relationship between actuators and syringe pumps, it provides a simple and accurate approach to building pneumatic soft robot control systems, eliminating the need for air compressors and valves.

II. ROBOT DESIGN AND FABRICATION

A. Design of Actuators

Inspired by the bending actuators fabricated from asymmetric beams and films [16], we redesigned two types of lightweight pneumatic bending actuators for the forward and turning motions of the soft robot. The soft robot includes three actuators, including a turning actuator and two locomotion actuators fixed

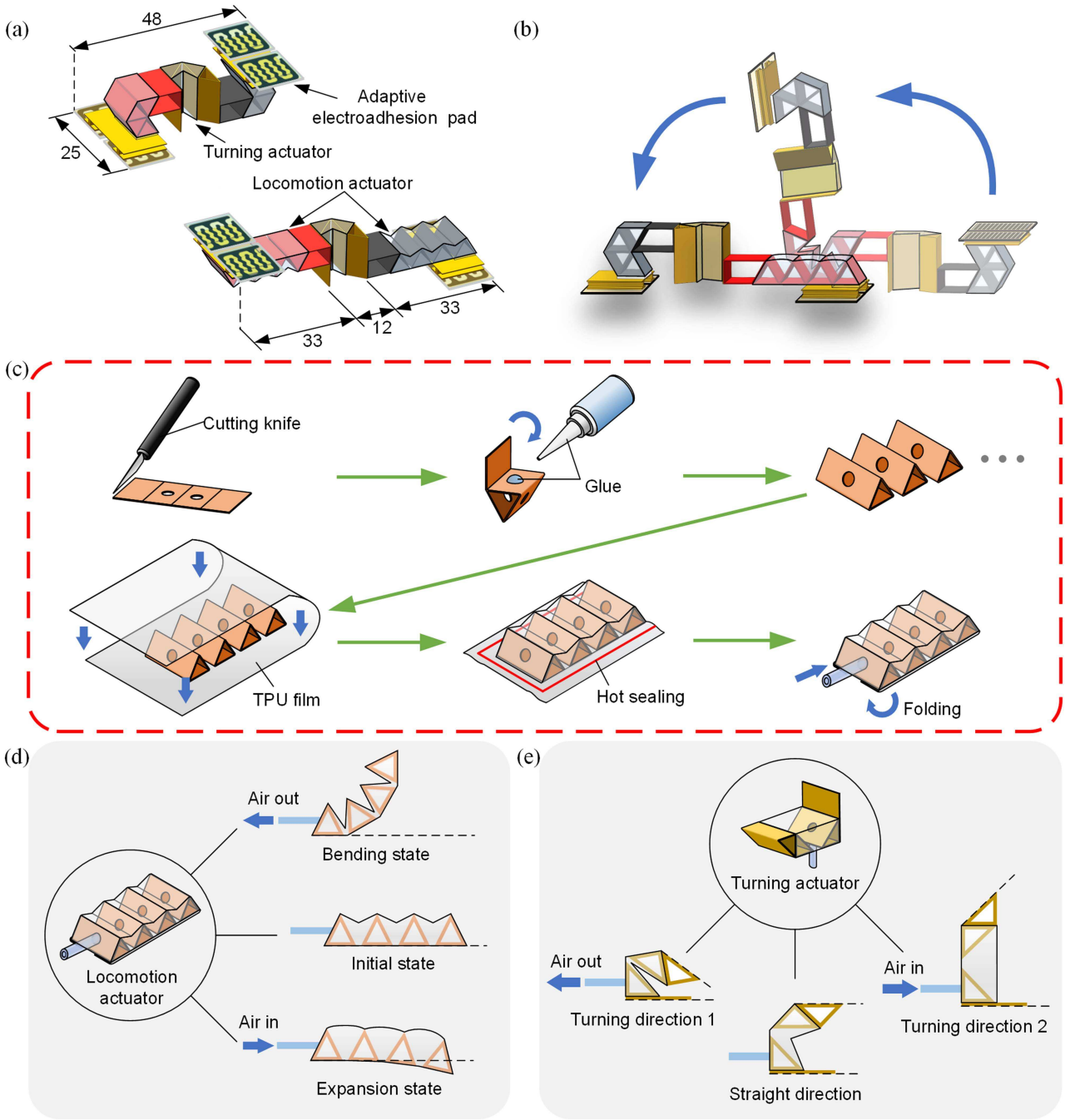

Fig. 1. Design and fabrication process of pneumatic actuators. (a) Composition and dimensions of the robot. The robot consists of two locomotion actuators, a turning actuator, and two adaptive EA pads. Unit: mm. (b) Schematic of the robot's motion actuated by one of the locomotion actuators. (c) Fabrication process for the locomotion actuator. The turning actuator is fabricated in the same way but with different dimensions. (d) Different states of the locomotion actuator determine how the robot moves. (e) Different states of the turning actuator determine the direction of the robot's movement.

at its two ends [Fig. 1(a)]. Each actuator consists of skeletons made of polyvinyl chloride (PVC) flakes and a thermoplastic polyurethanes (TPU) film. The skeletons are arranged in series and encased in a thin film to obtain stable and controllable bending deformations. Syringe pumps are used to control the actuators via connected silicone tubes. When the internal air pressure of the actuators is reduced, the pressure difference drives the film to shrink inward, bending to one side under the restraint of the skeletons.

The soft robot moves with the bending of the locomotion actuators, as shown in Fig. 1(b). Each locomotion actuator has four skeletons in the shape of regular triangular prisms, which are parallel. The lower surfaces and upper edges of these skeletons are bonded to the film so that the film's length is fixed between adjacent skeletons. The initial state of the actuator is defined when the lower surfaces of the four skeletons are in the same plane. At this point, the film between the upper edges of the adjacent skeletons is an inwardly concave arc. When the

internal air pressure of the actuator decreases, this part of the film shrinks into the space between the skeletons so that the upper edges of the skeletons approach each other and bend the actuator; when the internal air pressure increases, the film expands outward, and the actuator can bend slightly in the opposite direction [Fig. 1(d)]. Compared to most other pneumatic actuators [15], the hollow structure greatly reduces weight, while the triangular skeletons ensure structural strength.

The turning actuator controls the angle between the two locomotion actuators. The structure of the turning actuator is similar to the locomotion actuators. Two symmetrically arranged right-angled triangular prism skeletons are wrapped in a TPU film. In particular, the turning actuator has additional skeletons outside of the film. These extra skeletons allow the turning actuator to align its end-connected locomotion actuators in a straight line when bent to half of the maximum bend angle, a position we call the turning actuator's straight direction [Fig. 1(e)]. By this structure, the soft robot can achieve two-directional turning with a single turning actuator instead of using two parallel actuators [32], [33].

B. Materials and Fabrication of Actuators

PVC is used to fabricate the skeletons of the actuators because of its decent mechanical property and lightweight. A TPU film covers the PVC skeletons as skin. TPU can be sealed at a high temperature and is flexible enough for repeated bending. Since the structures of the locomotion and turning actuators are similar, the fabrication process of the locomotion actuators is mainly described here [Fig. 1(c)].

A 10 mm $\times$ 20 mm rectangle is cut from a 0.3 mm thick PVC flake. The rectangular PVC is divided into four areas along the long side by the scratches carved by the blade. In addition, holes with a diameter of 1 mm are punched in the center of the two central areas to allow air to go through. After that, the rectangle is folded into a triangular prism along the scratches and fixed with glue. The side length of the triangular prism skeleton is 5 mm, and the edge length is 10 mm. Four triangular prism skeletons are assembled to form one locomotion actuator.

The four skeletons are bonded straightly on a 0.08 mm thick TPU film by double-sided tape, with a 1.5 mm gap between the bottom edges of adjacent skeletons to facilitate the bending and folding of the thin film. The TPU film is folded from one end of the skeletons and covers all the skeletons. Then, the upper TPU film is glued to the upper edge of each skeleton.

Remarkably, the film's length between the edges of adjacent skeletons is about 1 mm longer than the linear distance between them. The two layers of the TPU film are sealed by a heat sealer at 130 °C. After trimming off the marginal TPU film, the remaining hems are folded to the bottom and bonded with tapes. Finally, a small hole with a diameter of 1 mm is punched into the film at one end of the actuator, connected with a silicone tube, and sealed with glue.

There are several differences in the fabrication of the turning and locomotion actuator. First, the shape of the skeletons of the turning actuator is an isosceles right-angled triangular prism with 5 mm right-angled sides and 10 mm edges. The two skeletons symmetrically adhere to the TPU film. Second, the film's length between the edges of the skeletons is equal to their linear distance. Third, after heat sealing, an isosceles right-angled triangular prism of the same size as the skeletons and a 10 mm $\times$ 10 mm flat is glued to both ends of the actuator. Finally, a silicone tube is attached to the bottom of the actuator.

Each locomotion actuator and the turning actuator are connected by a quadrangular prism with a right-angled trapezoid cross-section (5 mm topline, 7.5 mm baseline, and 4.3 mm height). The quadrangular prism is cut and folded from PVC flakes. The actuators and the connecting parts are fixed by double-sided tapes. The bending directions of the two locomotion actuators are opposite and perpendicular to the bending direction of the turning actuator.

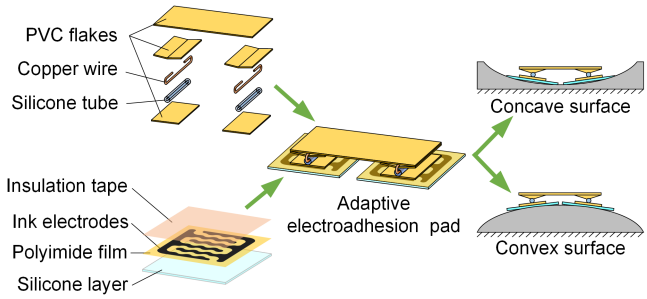

Fig. 2. Structure of adaptive EA pad. The adaptive EA pad can adapt to concave and convex surfaces due to two rotatable EA pads.

C. Design and Fabrication of Adaptive EA Foot Pad

EA will enable the overall lightweight and miniaturization of the robot due to its simple structure and decent adsorption performance [38]. To improve the surface adaptability and motion performance of the robot, we propose an adaptive EA foot pad that can adhere to curved surfaces. As illustrated in Fig. 2, the adaptive foot pad includes a backplane and two rotation shafts under the backplane. These shafts allow the two attached EA pads to rotate freely within a small range. When the adaptive foot pad touches a surface, the EA pads can autonomously rotate to the optimal contact angle to stably adhere to the surface.

An EA pad includes four parts: a polyimide substrate, a pair of interdigital conductive ink electrodes, an insulating tape, and a silicone film. When a high voltage is applied to the electrodes, the contact surface is polarized by a strong electrical field between the interdigital electrodes. The opposite charges in the polarized surface and the EA pad attract each other, resulting in adhesion force. The adhesion force can rapidly reduce within seconds after the voltage is turned OFF. It is difficult to provide stable adhesion force by a single EA for surfaces with rough or weak polarization properties, so a layer of silicone film is added to the EA pad to improve the adaptability. On the one hand, the EA force provides a preload to the silicone film to create elastomer adhesion to the contact surface; on the other hand, the elastomer adhesion can provide better peel strength and enhance the normal adhesion force, thus increasing the EA force [39].

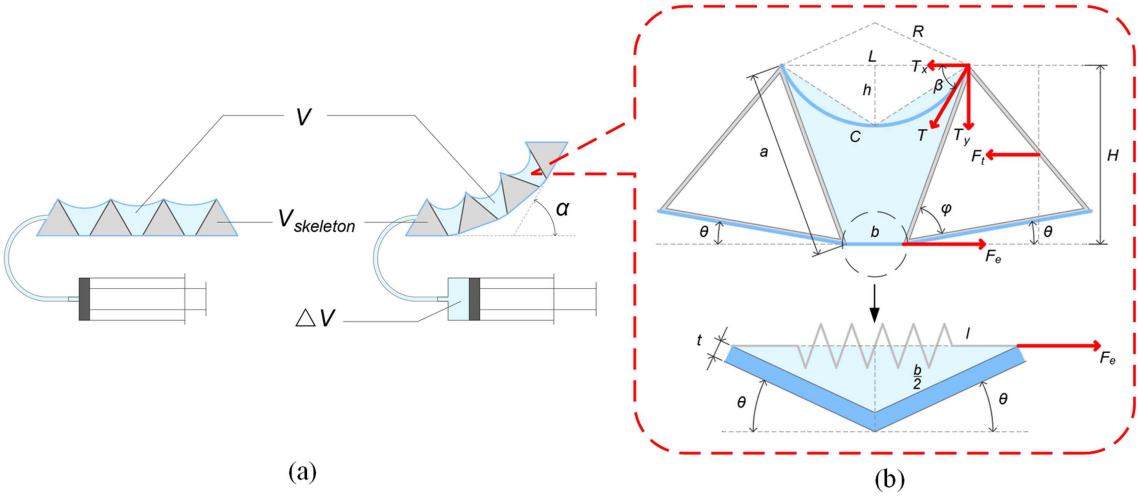

Fig. 3. Theoretical modeling of the actuators. (a) Schematic of the relationship between the actuator bending angle and the volume change of the syringe pump. (b) Analytical model of an actuator unit. Each unit consists of two triangular prism PVC skeletons and a part of TPU film connected between the two skeletons.

The adaptive foot pad is mainly made of PVC, the same as the actuators. A large rectangle (10 mm × 18 mm) and four small rectangles (5 mm × 10 mm) are cut from a 0.3 mm thick PVC flake, and two small rectangles are folded into a V shape along the long side. On the other two small rectangular PVC flakes, silicone tubes with a length of 10 mm are glued to the midline. The tubes are passed through by copper wires slightly longer than them. After that, the extra parts of the wires on both sides are bent by 180°. Finally, the bending parts of the copper wires are clamped between the large rectangular flake and the V-shaped flakes and fixed with glue. The distance between the two rotating shafts is 13 mm.

The EA pads are mainly made by silkscreen printing. First, a silkscreen with a pattern of the electrodes is pressed on a polyimide film used as the substrate. Then, the conductive ink is repeatedly scraped across the silk screen with a squeegee so that the ink can be penetrated by the electrode pattern and be printed on the substrate. The width of the interdigital electrodes and gaps is 1 mm, and the overall size of the electrodes is 11 mm × 12 mm. After drying in the air for 2–3 h, the electrodes are covered with insulating tape. The other side of the polyimide film is coated with Ecoflex-0030 silicone with a thickness of 0.25 mm and cured in an oven at 60° for 30 min. Finally, the EA pads are cut into a rectangle of 12 mm × 13 mm. Each EA pad is connected with the PVC flakes on the rotation shaft with double-sided tape.

III. Theoretical Analysis

A. Theoretical Modeling of Actuators

The relationship between the bending angle of the actuator and the volume change of the syringe pump under constant atmospheric pressure and temperature can be calculated by building a theoretical model [Fig. 3(a) and (b)]. We decompose one actuator of the robot into several units for analysis. Each unit includes two triangular prism PVC skeletons and a part of TPU film connected between the two skeletons. In a single unit, the TPU film is glued to the lower surface and upper edge of each prism skeleton without being fixed on the left and right sides. At the same time, the TPU film at the lower surface is thicker and has a larger elastic modulus due to the folding. We perform the analysis with a section parallel to the bending direction and ignore the effect of gravity to simplify the theoretical model. Furthermore, the part of the film on the left and right sides is ignored; the film on the upper side is modeled as a fixed, inextensible film at both ends, and the geometry approximates a parabola; the thicker film at the bottom is modeled as two symmetrical cantilever springs.

In the initial state, the lower surfaces of triangular prism skeletons are in the same plane. When bending occurs, the angle between the lower surface of each prism and its initial position is θ. Assuming that the bending condition of each unit is the same when the whole actuator is bent. The overall bending angle α of the actuator is defined as the angle between the lower surfaces of the prism skeleton at both ends, and the relationship between it and θ can be written as

$$\alpha = 2\,(N-1)\,\theta \tag{1}$$

where N is the number of skeletons that an actuator contains.

In the initial state, the internal pressure of the actuator is the external atmospheric pressure. Since the interior of the actuator and the connected syringe pump is a closed space, when the internal volume of the syringe pump is changed, the equation of pressure and volume change can be obtained by

$$P_0\,(V_0 + V_{\text{skeleton}}) = P\,(\Delta V + V + V_{\text{skeleton}}) \tag{2}$$

$$P = P_0 - \Delta P \tag{3}$$

where P_0 is the internal pressure of the actuator in the initial state, which can be regarded as the standard atmospheric pressure here ($P_0 = 0.1$ MPa). P and ΔP are the internal pressure and pressure difference between internal and external after bending, respectively. ΔV is the internal volume change of the syringe pump. V_{skeleton} refers to the total volume of the interior space

of the prism skeletons, which can be expressed as

$$V_{\text{skeleton}} = NWS_{\text{skeleton}} = \frac{1}{2}NWa^2 \sin\varphi \tag{4}$$

where S_{skeleton} is the sectional area of the interior space of the prism skeletons, W is the width of the skeletons, a is the side length of the triangle, and φ is the basic angle of the triangle. V represents the volume between the skeletons and the film after bending, and V_0 is the initial volume when the bending angle θ is 0. V can be calculated as

$$V = (N-1)\,WS \tag{5}$$

where S is the cross-sectional area between the prism skeletons and the film in each unit, which can be approximated as the area of the trapezoid $S_{\text{trapezoid}}$ minus the area of a small triangle, the S_{triangle}

$$S = S_{\text{trapezoid}} - S_{\text{triangle}} = \frac{1}{2}(L+b)\,H - \frac{1}{2}Lh \tag{6}$$

$$L = 2a\cos(\theta+\varphi) + b \tag{7}$$

$$H = a\sin(\theta+\varphi) \tag{8}$$

where L is the distance between the upper edges of adjacent skeletons, H is the height of the skeletons in the vertical direction, and B represents the film's length between the lower surfaces of adjacent skeletons. The length of the sides of the triangle area can be estimated as half of the film's arc length C; hence, the height h of the triangle can be calculated as

$$h = \sqrt{\left(\frac{C}{2}\right)^2 - \left(\frac{L}{2}\right)^2}. \tag{9}$$

Based on the parameters of a, b, and C determined in the manufacturing process, the relationship between V and the bending angle θ can be derived as

$$\begin{aligned} V = {} & \frac{(N-1)\,W}{2}\left(2a\cos(\theta+\varphi)+2b\right)a\sin(\theta+\varphi) \\ & - \left(2a\cos(\theta+\varphi)+b\right) \\ & \times \left(\left(\frac{C}{2}\right)^2 - \left(a\cos(\theta+\varphi)+\frac{b}{2}\right)^2\right)^{\frac{1}{2}}. \end{aligned} \tag{10}$$

Static analysis for the actuator unit can be operated under any bending angle. As the syringe pump changes its internal volume, a pressure difference is created between the inside and outside of the actuator, causing it to bend. In equilibrium, each unit mainly contains three forces in the horizontal direction

$$F_t + T_x = F_e \tag{11}$$

where F_t stands for the thrust force generated by the pressure difference ΔP acting on the section perpendicular to the bending direction, T_x is the film tension in the horizontal direction under the action of the pressure difference ΔP, and F_e is the elasticity of the bottom TPU film due to bending force. F_t can be calculated as

$$F_t = \Delta PHW. \tag{12}$$

The film tension T can be determined by Laplace's law

$$T = \Delta PRW \tag{13}$$

$$T_x = T\cos\beta \tag{14}$$

$$\beta = \cos^{-1}\frac{L}{2R} \tag{15}$$

where T_x is the component force of the tension T in the horizontal direction, β represents the angle between the two directions, and R is the radius of curvature of the film at the fixed position of the skeleton's upper edge. Since R can be eliminated from (13) to (15), T_x becomes

$$T_x = \frac{1}{2}\Delta PWL. \tag{16}$$

The elastic force F_e generated by the bending of the bottom TPU film can be estimated by the cantilever spring model as

$$F_e = k\Delta l = k\,(l_0 - l) \tag{17}$$

$$l = \frac{b}{2}\cos\theta \tag{18}$$

$$k = \frac{EWt^3}{4\left(\frac{b}{2}\right)^3} = \frac{2EWt^3}{b^3} \tag{19}$$

where l is the projection of the length of the cantilever spring on one side in the horizontal direction, and l_0 is the length of l when the bending angle θ is 0 ($l_0 = b/2$). The parameter k is the elastic modulus of the TPU film at the bottom, E refers to its elastic modulus, and t is the thickness of the film. The elastic modulus E can be approximated by calculating the ratio of the stress to the strain rate of the film. Combining (11)–(19), the relationship between the pressure difference ΔP and the bending angle θ can be written as

$$\Delta P = \frac{Et^3\,(1-\cos\theta)}{b^2\left(a\sin(\theta+\varphi) + a\cos(\theta+\varphi) + \frac{b}{2}\right)}. \tag{20}$$

By substituting (10) and (20) into (2), we can obtain the relationship between the volume change ΔV of the syringe pump and the bending angle θ, and then combine (1) to further obtain the relationship between the overall bending angle α and ΔV. The relevant calculation parameters of the theoretical models of the locomotion actuator and the turning actuator are shown in Table II. By using this theoretical model, it becomes possible to calculate the required volume change of the syringe pump required for each actuator to achieve the specified bend angle. This allows for the decomposition of the motion control of the robot into a combination of bend angle control of its three actuators.

B. Robot Workspace

The kinematic model of the soft robot can be established by considering the midpoints of the TPU films connecting the skeletons as joints. As shown in Fig. 4(a), the base coordinate system and the coordinate system of each joint are established, in which the joints of the two locomotion actuators can rotate in the x–z plane, and the joints of the turning actuator can rotate in the y–z plane. Assuming that the bending of each actuator is

TABLE II
PARAMETER TABLE FOR THEORETICAL MODELING OF THE ACTUATORS

Parameter	N	W/mm	a/mm	b/mm	C/mm	φ/°	t/mm	E/MPa
Locomotion actuator	4	10	5	1.5	7.5	60	0.2	390
Turning actuator	2	10	7.1	1.5	11.5	45	0.2	390

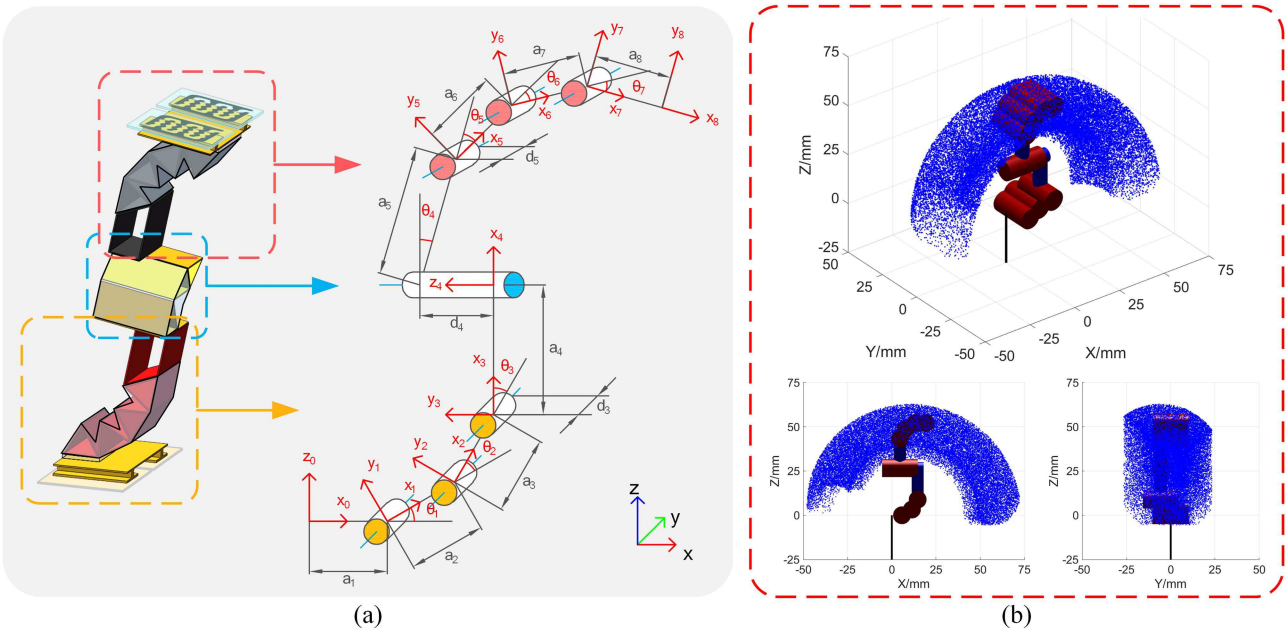

Fig. 4. Kinematic model of the robot. (a) Simplified robot kinematics model was obtained by considering the TPU films between skeletons as joints. (b) Workspace of one robot's end when the other end adheres to a wall. The set of blue dots indicates most of the accessible positions of the end.

uniform. The angles of the adjacent links between the joints are θ_1–θ_7, and the overall bending angles of actuators are α_1, α_2, and α_3, respectively, which can be expressed as

$$\theta_1 = \theta_2 = \theta_3 = \frac{\alpha_1}{3} \tag{21}$$

$$\theta_4 = \alpha_2 \tag{22}$$

$$\theta_5 = \theta_6 = \theta_7 = \frac{\alpha_3}{3}. \tag{23}$$

The length of the links between the joints are a_1–a_8, where a_1–a_3 and a_6–a_8 can be estimated from the geometric parameters a and b of the locomotion actuators. Meanwhile, a_4 and a_5 are determined by the parameters of the turning actuator and the connecting parts between the actuators, where $a_4 = 17.75$ mm and $a_5 = 16.75$ mm. The parameters d_1–d_8 stand for the distances between the links, where d_1, d_2, and d_6–d_8 take 0 since the adjacent links are coplanar. Apart from this, d_3 and d_5 are the offsets of the connecting parts between the actuators, taking 5.6 mm, and d_4 represents the width W of the turning actuator. The D-H parameter table of the robot is shown in Table III. Assuming that one end of the robot is adsorbed on a wall, the other end can be shifted to the specified position by controlling the bending angle of each actuator to achieve moving or transition. The base coordinate system is established with the fixed end as the coordinate origin according to the known D-H parameters. The coordinates of the terminal joint can be calculated through

TABLE III
D-H PARAMETERS

Link #	θ_i	d_i	a_i	α_i
1	$\alpha_1/3$	0	$a+b/2$	$-\pi/2$
2	$\alpha_1/3$	0	$a+b$	0
3	$\alpha_1/3$	d_3	$a+b$	0
4	α_2	W	a_4	$\pi/2$
5	$\alpha_3/3$	d_5	a_5	$-\pi/2$
6	$\alpha_3/3$	0	$a+b$	0
7	$\alpha_3/3$	0	$a+b$	0
8	0	0	$a+b/2$	0

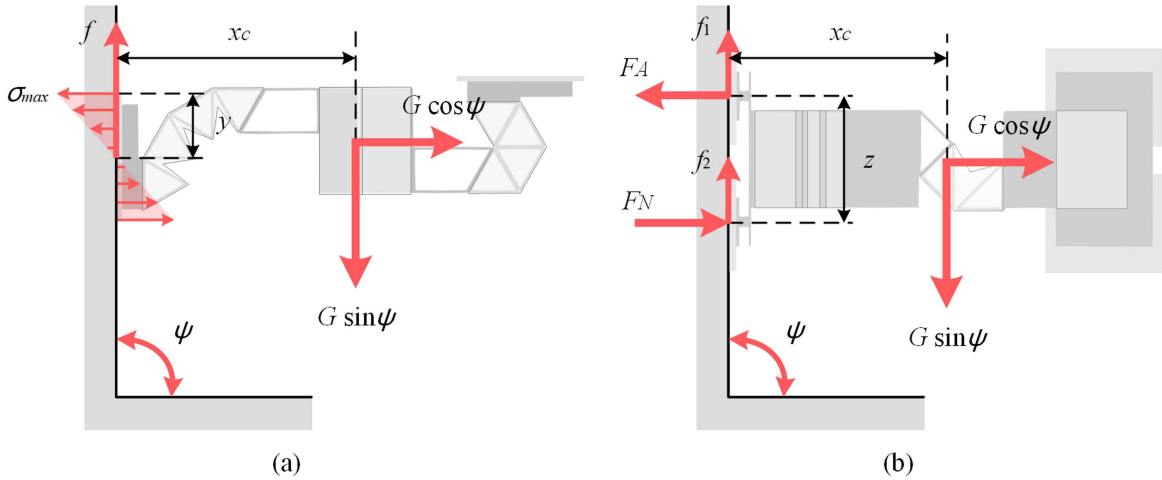

Fig. 5. Free body diagram for adhesion stability analysis. (a) Soft robot adheres to a wall when its body is perpendicular to the wall. (b) Soft robot adheres to a wall after turning 90°.

the forward kinematics. The transformation matrix from coordinate system $i-1$ to coordinate system i can be expressed as

$$ {}^{i-1}_{i}T = \begin{bmatrix} \cos\theta_i & -\sin\theta_i\cos\alpha_i & \sin\theta_i\sin\alpha_i & a_i\cos\theta_i \\ \sin\theta_i & \cos\theta_i\cos\alpha_i & -\cos\theta_i\sin\alpha_i & a_i\sin\theta_i \\ 0 & \sin\alpha_i & \cos\alpha_i & d_i \\ 0 & 0 & 0 & 1 \end{bmatrix}. \tag{24} $$

The coordinates of the terminal joint in the base coordinate system can be expressed as

$$ \begin{bmatrix} x \\ y \\ z \\ 1 \end{bmatrix} = \prod_{i=1}^{8} {}^{i-1}_{i}T \begin{bmatrix} 0 \\ 0 \\ 0 \\ 1 \end{bmatrix}. \tag{25} $$

On this basis, given the bending angle range of the three actuators, the coordinates of many points that can be reached by the terminal can be calculated. These points can be approximately regarded as the robot's working space [Fig. 4(b)]. The robot can meet various work requirements in this workspace by moving, turning, and transitioning.

In addition, the angle γ between the fixed end and the other end of the robot in the x-z plane can be calculated as

$$ \gamma = -\alpha_1 + \alpha_3 \tag{26} $$

which provides a theoretical basis for the required bending angles of the two locomotion actuators when transitioning between walls with different pinch angles, since the robot needs to attach its two end adsorption pads to the walls during the transition.

C. Adhesion Stability Analysis

The adhesion stability should be analyzed to ensure the soft robot can climb in different directions on walls with various inclination angles. Since the soft robot climbs by flipping, it is analyzed when its body flips perpendicular to the wall.

As illustrated in Fig. 5(a), the soft robot adheres to a wall at an inclination angle ψ. G is the gravitational force on the robot. The distance from the center of gravity to the footpad, x_c, can be approximated by the structural parameters of the soft robot. And y refers to half the length of the EA pad. The maximum normal adhesion stress σ_1 occurs at the top edge of the EA pad, which can be calculated as

$$ \sigma_1 = \frac{G\sin(\psi)\, x_c y}{2I} + \frac{G\cos(\psi)}{2A} \tag{27} $$

where I is the second moment of area of the EA pad cross-section and A is the area of a single EA pad. Fig. 5(b) illustrates the situation when the soft robot turns 90° in one direction. F_A is the adhesion force generated by the top EA pad, F_N is the normal force acting on the EA pad below, and z stands for the distance between the central axis of two EA pads. In this case, the moment balance equation can be expressed as

$$ F_A z = G\sin(\psi)\, x_c + G\cos(\psi)\frac{z}{2} \tag{28} $$

$$ F_A = \sigma_2 A \tag{29} $$

where σ_2 refers to the normal adhesion stress on the top EA pad. To ensure that the robot does not slip off the wall, its shear adhesion force must satisfy

$$ f \geq G\sin(\psi) \tag{30} $$

$$ f_1 + f_2 \geq G\sin(\psi) \tag{31} $$

where f is the total shear adhesion force on the EA pad in Fig. 5(a), and f_1 and f_2 are the shear adhesion forces on the upper and lower EA pads, respectively, in Fig. 5(b).

The range of normal and shear adhesion stress required for the soft robot to climb on a wall with an arbitrary inclination angle can be obtained by (27)–(31). The adhesion stability of the soft robot is ensured when the actual adhesion stress exceeds the maximum value of this range.

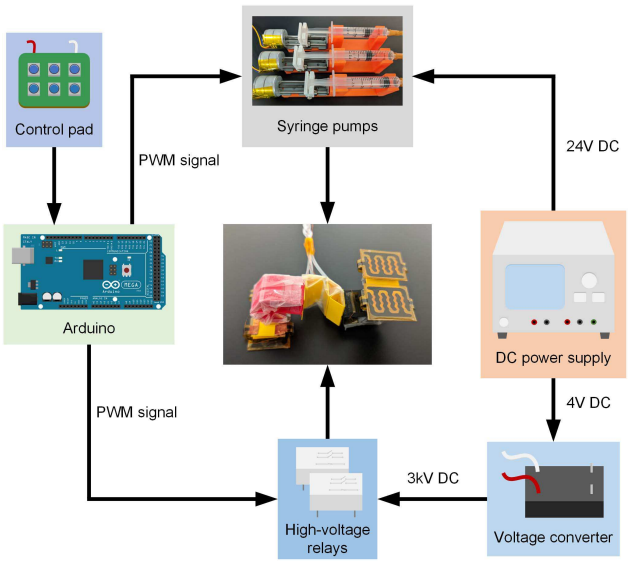

Fig. 6. Schematic of the control system. A dc power supply powers both the syringe pumps and the EA pads. A controller board provides control signals to the motors of syringe pumps and high-voltage relays to control the actuators and the EA pads.

IV. Experimental Setup

A. Control System

The soft robot is controlled in an open-loop manner, with the control system depicted in Fig. 6. Each actuator is controlled by a syringe pump consisting of a micro slide table with a stepping motor, a syringe, and a 3-D-printed stand. The plungers of the syringes are attached to the slide tables, allowing the volume change of each syringe to be determined by the corresponding displacement of the slide table. This establishes the relationship between the flexure of the actuators and the slide tables. A high-voltage converter module (EMCO E101, XP Power) amplifies a 4 V dc voltage to 3 kV, which is then transferred to each group of EA pads through two high-voltage relays (CRSTHV-2A, CRST RELAY). The syringe pumps are supplied with 24 V from a dc power supply (SPD3303X-E, SIGLENT), while the high-voltage converter module is supplied with 4 V.

A commercial controller board (Arduino Mega 2560) is utilized to provide the control signals. The Arduino sends signals to control the movement of the stepping motors in the syringe pumps and the opening and closing of the high-voltage relays. For the known work scenarios, the robot's movements can be planned in advance, and the required actuator bending angles can be determined for each movement. The corresponding volume changes can then be derived from the theoretical model to determine the output signals from the Arduino to the syringe pumps. A control pad with buttons is also connected to the Arduino to manually activate control signals in complex scenarios.

B. Motion Mechanisms

Here, we introduce three motion mechanisms of the robot: linear motion, transition motion between walls, and turning motion.

Fig. 7(a) shows examples of forward and backward linear motion on a vertical wall. This motion mode is also suitable for horizontal walls, inverted walls, inclined walls of various angles, and curved surfaces:

1) Steps of forward motion: In the first step, locomotion actuator A is on top, locomotion actuator B is on the bottom, and both are in a state of maximum bending. At this time, pad A, connected to the locomotion actuator A, is activated, and adsorbed on the wall. In the second step, the locomotion actuator A begins to straighten gradually from the bent state, thereby driving the robot to flip in the direction of movement. In the third and fourth steps, pad B, connected to the locomotion actuator B, contacts the wall and switches on the voltage to complete the adsorption process. Then, the voltage of pad A is turned OFF to achieve desorption. During this process, the locomotion actuator B is extended to the maximum extent, creating a slight arc toward the wall. This arc can ensure that the EA pad on the upper end has complete contact with the wall and make the EA pad on the lower end desorb easily after the voltage is turned OFF. In the last step, the locomotion actuator A is bent to the state it was in the first step. At this point, locomotion actuator B is on the upper side, and locomotion actuator A is on the bottom. Next, the robot completes a 180° flip motion in the direction of linear motion and enters the next motion cycle.

2) Steps of backward motion: In the first step, locomotion actuator B is on top, and pad B is activated. In the second and third steps, the locomotion actuator A is straightened, and pad A adheres to the wall when its voltage is switched ON. In the fourth step, after disconnecting the voltage from pad B, the locomotion actuator B extends slightly to allow pad B to detach from the wall. In the last step, the locomotion actuator A is bent back to its initial state, causing the robot to flip 180° backward and enter the next motion cycle.

As for transitioning motion, we perform a transition between two perpendicular walls as an example, as shown in Fig. 7(b). In the first step, assume that the robot adheres to a horizontal wall with the same state as in the first step of linear motion. In the second step, the locomotion actuator A extends, flipping the robot to the vertical wall until the upper edge of the EA pad B contacts the vertical wall. In the third step, the locomotion actuator B is slightly extended, and the angle of the EA pad attached to it is adjusted to be parallel to the vertical wall. Meanwhile, the vertical wall is adsorbed by pad B as the voltage is turned ON. In the fourth step, the locomotion actuator A extends to make pad A desorbed from the horizontal wall after the voltage is turned OFF. Finally, the locomotion actuator A is bent to the state in the first step, and the robot completes the transition from the horizontal to the vertical wall. This motion mode can be used for transitions between perpendicular walls and walls with an included angle of less than 180°. Assuming that the angle between the two walls is ψ and combining (26), the bending angles α_1 and α_3 of the two locomotion actuators in the third step can be determined according to the constraint $\gamma = -\alpha_1 + \alpha_3 = \psi$.

Turning motion is a combination of linear motion and motions of the turning actuator, as shown in Fig. 7(c). In the first step, it is assumed that the robot's state is the same as the first step of

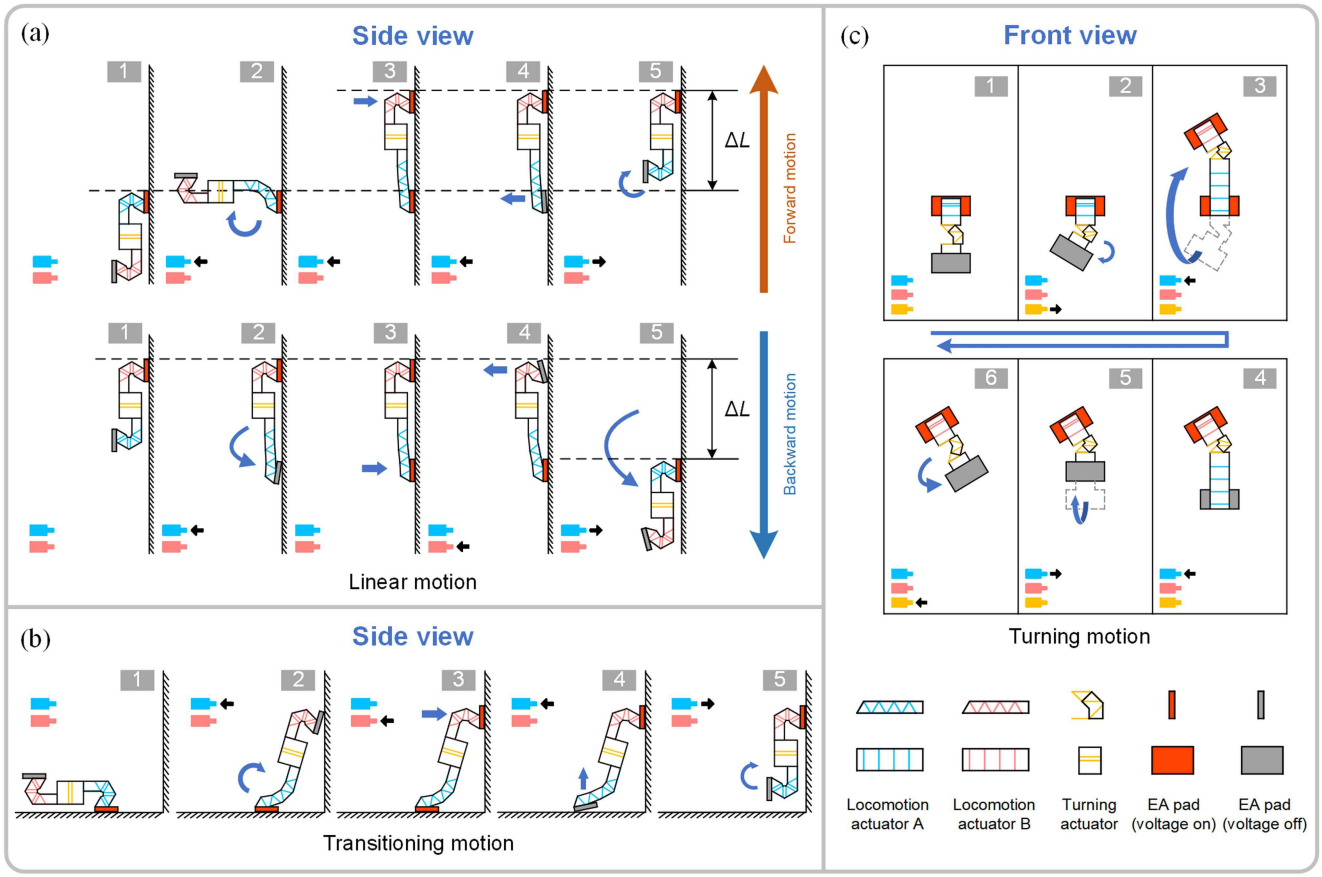

Fig. 7. Mechanisms of different motions. (a) Schematic of linear motion, including forward and backward motions, on a vertical wall. The same motion can also be performed on horizontal walls, inverted walls, inclined walls of various angles, and curved surfaces. (b) Schematic of transitioning motion between a vertical wall and a horizontal wall. (c) Schematic of turning motion. Both clockwise and counterclockwise turning are achievable. The different colored rectangles in the schematic diagrams represent the actuators of the corresponding color, and the black arrows indicate the air flowing into or out of the actuators.

the linear motion. In the second step, the turning actuator bends to create a certain angle between the locomotion actuators A and B. The bending direction and angle depend on the target direction. The third to fifth steps of turning motion are the same as the second to fifth steps of linear motion. However, due to the bending of the turning actuator, the locomotion actuator B and the connected pad B are turned to the target direction after being turned over. In the final step, the turning actuator is adjusted according to the direction of motion for the next cycle.

V. Experimental Results

The use of EA provides a small-sized and lightweight adsorption solution for the robot and enables the overall size and mass of the robot to be controlled within a small range. During motions, stable adhesion force can be generated by EA between the robot and various surfaces. Meanwhile, the lightweight structure of the robot can effectively prevent it from overturning and falling off. These characteristics allow the robot to perform various motions to achieve different functions.

First, characterization experiments were conducted on the actuators and EA pads. Then, a series of experiments were conducted to demonstrate the robot's versatile motions, including the linear motion on walls with different angles, the transition between walls, turning in different directions, and the combinations of the three motion modes. As mentioned above, the voltage of EA was 3 kV in the experiment to improve the service life and reduce power consumption. The airflow rate of each syringe pump was kept at about 262.5 mm^3/s, the maximum rate the pump motor can output stably.

A. Characterization of Actuators

A simple experiment was conducted to characterize the relationship between the syringe pump's volume change and the actuator's bending angle [Fig. 8(a)]. Meanwhile, the theoretical relationship can be obtained from (1) and (2). The comparisons between the theoretical model and the experimental results of the two actuators are shown in Fig. 8(b) and (c).

From the results, it can be concluded that our theoretical model is in good agreement with the experimental results. For example, the locomotion actuator achieved a bending angle of about 178° when the volume change of the syringe pump was 550 mm^3, and the turning actuator achieved a bending angle of about 78° with a volume change of 800 mm^3. The discrepancy between the experimental results and the theoretical model might be due to the folds created by the TPU film during the bending of the actuator, which created additional drag and blocked adjacent skeletons from further approaching each other.

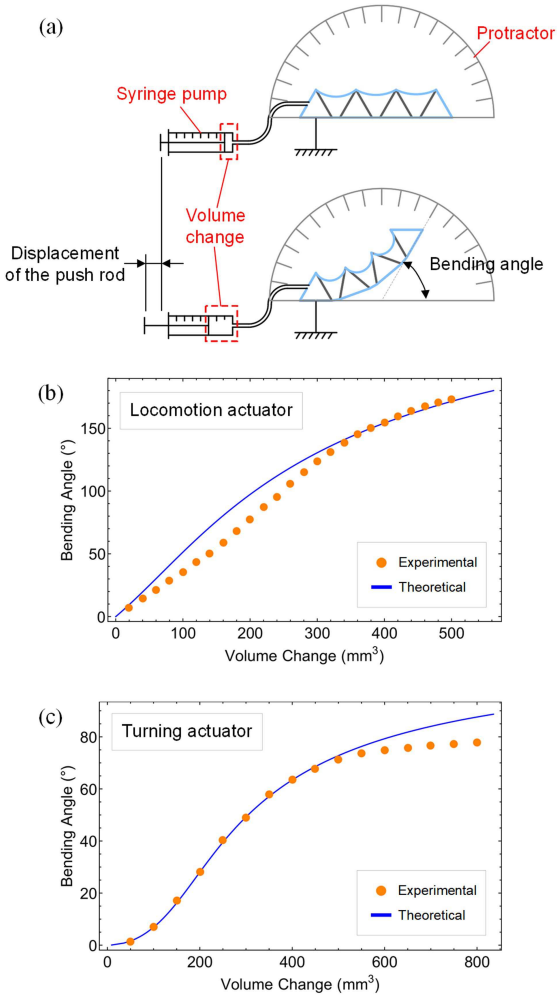

Fig. 8. (a) Schematic of the actuator's bending experiment. The syringe pump's volume changes with the displacement of the push rod, thus changing the bending angle of the actuator. The syringe pump's volume change and the corresponding bending angle of the actuator are recorded. (b) Comparison of the theoretical model and experiment results of the locomotion actuator. (c) Comparison of the theoretical model and experiment results of the turning actuator.

B. Characterization of the EA Pad

Using a simple measurement platform, we measured the normal and shear adhesion stresses of the fabricated EA pad under different conditions, as shown in Fig. 9(a).

First, the adhesion stress of the EA pad with and without silicone film was measured on a glass substrate under a series of incremental charging times at a voltage of 3 kV. The experimental results are illustrated in Fig. 9(b), showing that the EA pad with silicone film generated higher shear and normal stress. Furthermore, the adhesion stress of the EA pad without silicone film reached saturation after about 1 s of charge and did not rise much afterward, while the EA pad with silicone film continued to increase its adhesion stress even after 8 s. It took time for the silicone film to fully adhere to the substrate under the effect of electrostatic force, which explains why the adhesion stress continued to increase during this time.

Second, four common materials were selected as substrates to measure the adhesion stresses, including glass, aluminum, tile, and cardboard. Through a series of preliminary tests, three voltages of 0, 3, and 4 kV were finally chosen under the condition of ensuring a pronounced adhesion effect and no breakdown risk. The charging time was 5 s for each test. As shown in the results [Fig. 9(c)], when the voltage was turned OFF, the generated normal stress of the EA pad on the four materials was around 0.2–0.3 kPa, while the shear stress on other materials except cardboard was slightly larger than the normal force. The shear stress on the cardboard was close to 0.5 kPa, which was more than twice the normal stress since the surface of the cardboard was rougher and softer than other materials. When a voltage of 3 or 4 kV was applied, the normal stress could reach about 1.2–1.5 kPa, and the shear stress could reach about 2.1–2.5 kPa. It can be seen from the measurement results that the normal stress and shear stress of the EA pad at 3 kV were about 5–7 times that of the power-OFF state. The adhesion stress had a large difference between the high voltage and power-OFF conditions, which was beneficial to stable adsorption and desorption of the robot during motion. The adhesion stress at 4 kV was only about 10% more than that at 3 kV. Therefore, to reduce power consumption and improve service life, 3 kV was usually used when the robot was working. Fig. 9(d) illustrates the comparison of the soft robot's normal stresses on four materials under 3 kV and the range of required normal stress, which can be obtained from (27) to (29). In addition, from the results, it can be easily concluded that the shear force is much higher than the robot's self-weight, satisfying (30)–(31). The adhesion capacity was enough to support the soft robot to achieve stable motion on horizontal, vertical, and inverted surfaces.

We also measured the normal adhesion stress on surfaces with different curvatures to verify the EA pad's curved-surface adaptability. As shown in Fig. 10(a), a piece of cardboard was attached to a 3-D-printed curved surface as the substrate. Convex and concave surfaces with curvatures of 5, 10, 15, and 20 m^{-1} were used here. The results show that the adsorption stress of the EA pad decreases with increasing surface curvature. As the two adhesion films in the pad are flat and have limited rotation, the EA pad has a limited range of curvature adaptability. Therefore, if the curvature of the surface is greater than the adaptation range of the EA pad, the effective adsorption area will be reduced, resulting in low adsorption stress. Comparing the results with the theoretical maximum required stress [Fig. 10(b)], the adaptive EA pad could provide enough adhesion stress on convex surfaces with curvatures from 5 to 15 m^{-1} and concave surfaces with curvatures from 5 to 20 m^{-1}.

C. Linear Motion

Fig. 11 illustrates the two linear motions of the robot. We assumed that the red locomotion actuator and the EA pad connected to it were "locomotion actuator A" and "EA pad A," the black one on the other side and the EA pad connected to it were "locomotion actuator B" and "EA pad B."

1) Forward Motion: The timelines of the volume change of syringe pumps and the voltage state of the two adsorption pads are plotted in Fig. 11(a). It is demonstrated in Fig. 11(b) that the robot moved forward on a horizontal wall and completed two

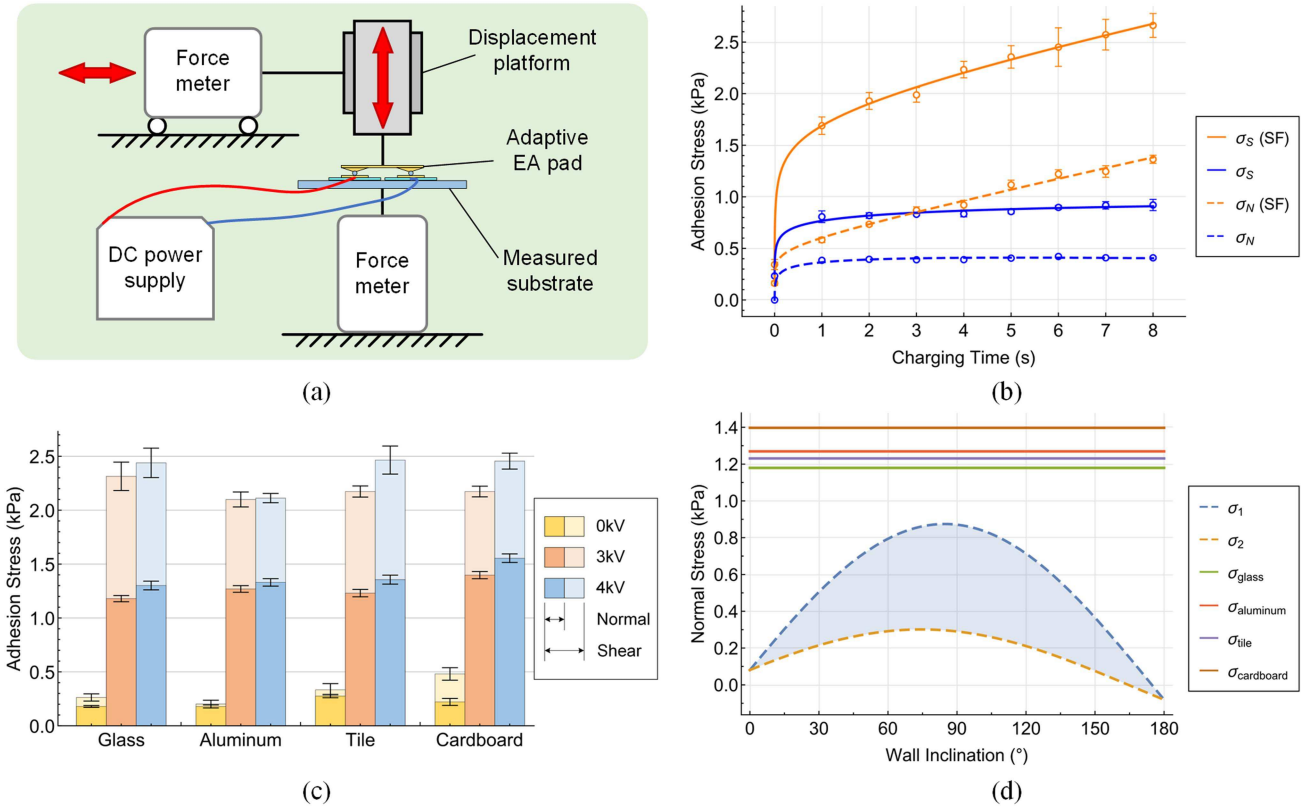

Fig. 9. (a) Schematic of the adhesion stress measurement experiment. The normal stress and the shear stress are measured, respectively, by two force meters. (b) Characterization of the adhesion stress of the EA pad with and without silicone film at different charging times. σ_S and σ_N represent shear stress and normal stress, respectively. "SF" denotes the adhesion stress measured with the EA pad with silicone film. (c) Adhesion normal and shear stress of the EA pad on glass, aluminum, tile, and cardboard under different voltages. (d) Theoretically required adhesion normal stress on inclined walls, and the experiment results on different materials under 3 kV.

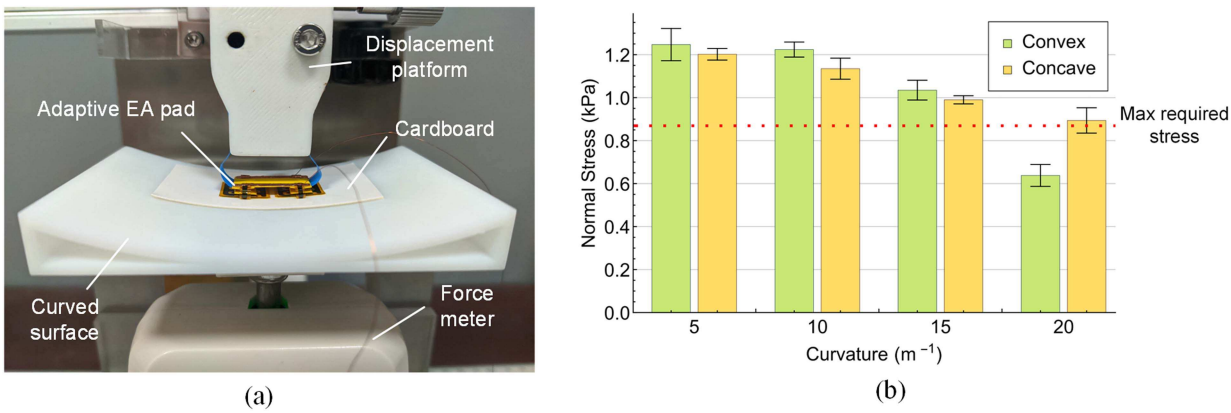

Fig. 10. (a) Adhesion normal stress measurement of the adaptive EA pad on curved surfaces. (b) Measurement results on convex and concave surfaces with different curvatures.

motion cycles consecutively. Initially, the locomotion actuator A was in front, and the EA pad A was adsorbed on the wall under a voltage of 3 kV. Then, the robot completed a 180° flip driven by the locomotion actuator A, thus moving a large step forward. After that, EA pads A and B switched their energized states so that A was desorbed, and B was adsorbed to the wall after a 5 s charge. Finally, the locomotion actuator A returned to its initial state. This motion cycle took about 13 s, and the two locomotion actuators worked alternately in each cycle. The robot moved about 50 mm in each motion cycle, and the average moving speed was about 3.85 mm/s (0.08 body length/s).

As shown in Fig. 11(c) and (d), the robot also had the ability to move on vertical and inverted walls. Due to the advantage of light weight and stable adhesion, the robot could move in precisely the same steps as on the horizontal wall in both cases, resulting in no speed reduction. In addition, it can be observed that the robot's body sagged when moving on the inverted wall,

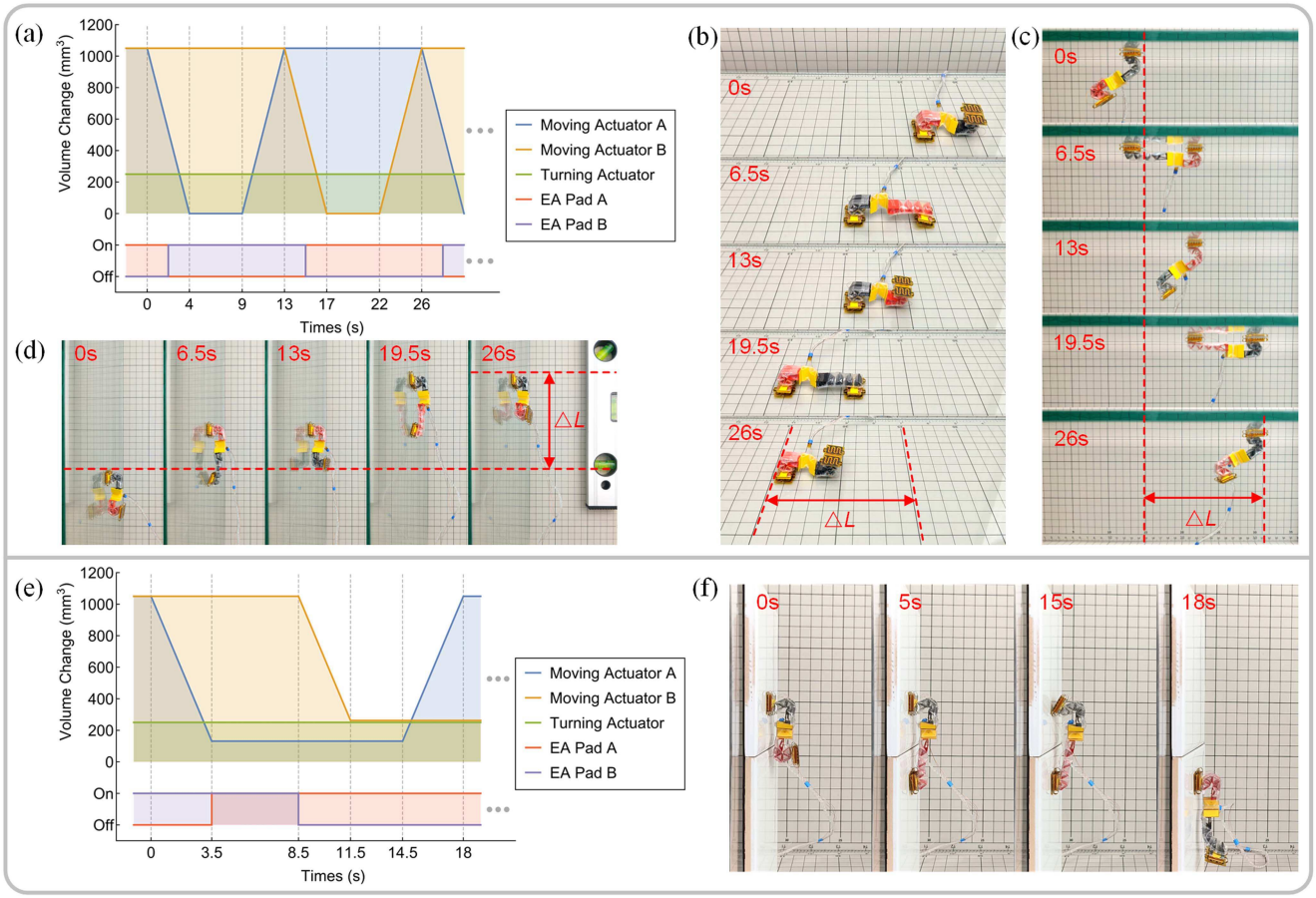

Fig. 11. Demonstrations of linear motion, including forward and backward motions. (a) Timeline of the state of the control system for forward motion. The locomotion actuators move alternately to complete two motion cycles. (b) Forward motion of the robot on a horizontal wall. (c) Forward motion of the robot on an inverted wall. (d) Forward motion of the robot on a vertical wall. (e) Timeline of the state of the control system for backward motion. (f) Backward motion of the robot on a vertical wall.

which was caused by gravity and the robot's softness and had no adverse effect on its motions.

With this flip-forward motion, the robot could move at a similar speed with a lower motion frequency to the soft robots with an inchworm-type motion [29], [33]. Our future article aims to further increase the speed of the robot's movement by increasing the frequency of its flips.

2) Backward Motion: The flipping motion proved reversible and beneficial to the robot's flexibility. The timelines of the control system for backward motion are potted in Fig. 11(e). Fig. 11(f) presents the backward motion of the robot on a vertical wall. In the initial state, the voltage of EA pad B was ON and the robot was adsorbed on the wall. The locomotion actuator A was straightened to allow EA pad A to touch the wall. After the EA pad A had reached stable adsorption, a certain amount of air was injected into the locomotion actuator B to generate a peeling force for the EA pad B to peel off the wall.

Finally, the locomotion actuator A bent and flipped the robot 180° to complete a backward motion cycle. The average backward speed was about 2.78 mm/s (0.058 body length/s).

D. Transitioning Motion

The robot can transition from one wall to another to expand its reachable space. This transitioning motion is achieved by flipping the robot's body, which is similar to linear motion.

Fig. 12(a) and (b) illustrates the timeline of the control system and the experiment results of the robot transitioning from a horizontal to a vertical wall. Initially, the robot was close to the corner between the two walls. The locomotion actuator A was then expanded until the EA pad B touched the vertical wall, at which point the bending angle of the locomotion actuator A reached about 73°. Afterward, the voltage of the EA pad B was switched ON, and a small amount of air was injected into the locomotion actuator B to make the bending angle reach about 163° so that the EA pad B was parallel to the vertical wall according to the constraint $\gamma = -\alpha_1 + \alpha_3 = 90°$. In the next step, under the combined effect of the EA forces and the expansion of actuator A, the EA pad B completely adsorbed the vertical wall. Meanwhile, the EA pad A was separated from the horizontal wall. Finally, the locomotion actuator A was bent to the initial state after 4–5 s of charging. The transitioning motion from the horizontal to the vertical wall took about 15 s.

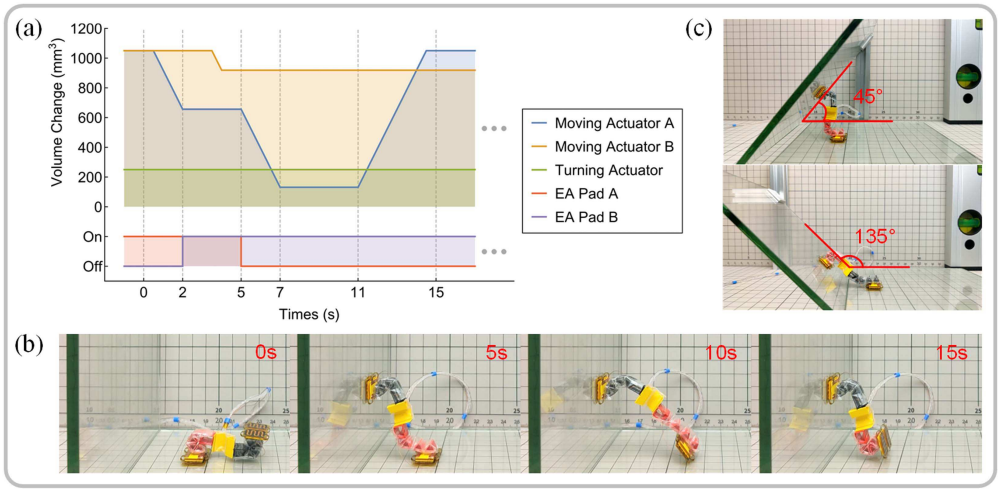

Fig. 12. Demonstrations of transitioning motion. (a) Timeline of the control system state when the robot transitions between two mutually perpendicular walls. (b) Transitioning motion of the robot from a horizontal wall to a vertical wall. (c) Transitioning motion between walls with an included angle of 45° and 135°, respectively.

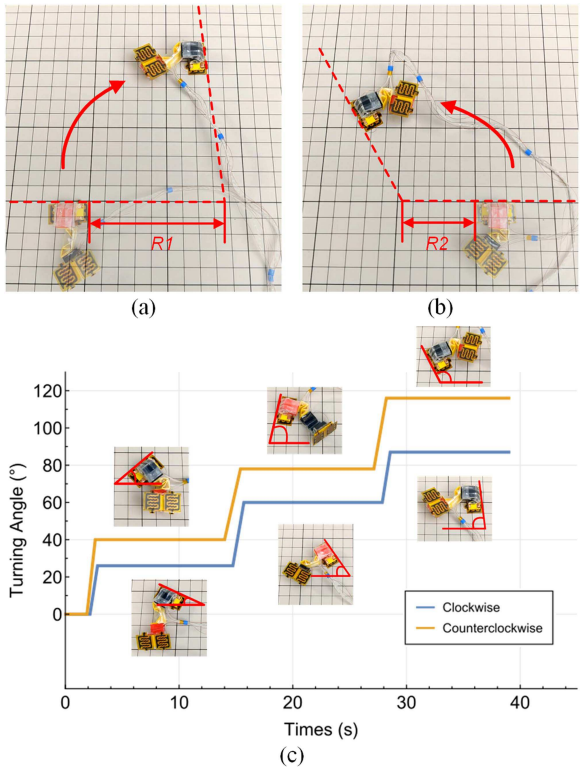

Fig. 13. Demonstrations of the robot turning in two directions. The minimum turning radius and speed are different in the two cases. (a) Turning motion in a clockwise direction. (b) Turning motion in a counterclockwise direction. (c) The experimental results of the turning angle in two directions as a function of time.

The robot can also accomplish transitions between walls with other angles within 180°. The experiments of transitioning between walls with an included angle of 45° and 135° were carried out, respectively. As shown in the top figure of Fig. 12(c), the bending angles of the two locomotion actuators were about 98° and 143°, following the constraint $\gamma = -\alpha_1 + \alpha_3 = 45°$. And the bending angles of the two locomotion actuators were about 45° and 180° in the lower figure of Fig. 12(c), which followed the constraint $\gamma = -\alpha_1 + \alpha_3 = 135°$.

By controlling the bending angle of the two actuators in real time, the soft robot can readily make quick transitions between different surfaces in unstructured environments.

E. Turning Motion

The turning motion of the robot in the specified direction is achieved by adjusting the bending angle of the turning actuator before each motion cycle. Due to the asymmetric structure of the turning actuator, the minimum turning radius and corresponding turning speed of the robot are different in two directions.

To measure the minimum turning radius and speed, the robot performs three motion cycles on a wall with the maximum expansion and bending state of the turning actuator, respectively. It is shown in Fig. 13(a) and (b) that the soft robot turned clockwise when the turning actuator was in the maximum expansion state, the minimum turning radius R_1 was about 85 mm (1.77 body length), and the average turning speed was 2.23 °/s; the soft robot turned counterclockwise when the turning actuator was in the maximum bending state, the minimum turning radius R_2 was about 52 mm (1.08 body length), and the average turning speed reached 2.97 °/s.

F. Application Demonstration

Some potential applications of the robot based on the combination of the various motion capabilities described above are demonstrated in Fig. 14. Fig. 14(a) shows that the robot successfully moved from a horizontal wall to the ceiling through linear and transitioning motion. The addition of the turning function further expands the reachable space of the robot. As shown in Fig. 14(b), the robot accomplished a series of motions on three perpendicular walls. The robot transitioned from a horizontal to a vertical wall and completed a 90° turn on the vertical wall. After that, it transitioned again to move

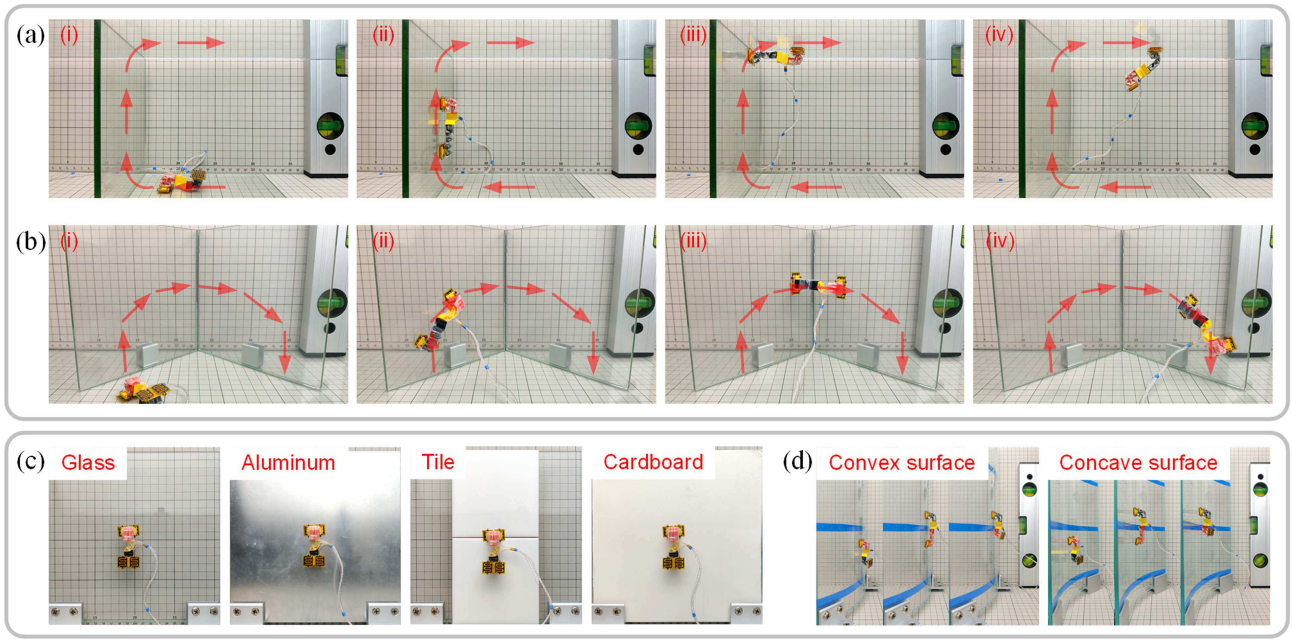

Fig. 14. Motions of the robot in complex environments. (a) Moving from a horizontal wall to the ceiling through linear and transition motions. (b) Moving on three perpendicular walls with linear, transitioning, and turning motions. (c) Climbing on vertical walls made of glass, aluminum, tile, and cardboard. (d) Climbing on a convex surface and a concave surface, respectively.

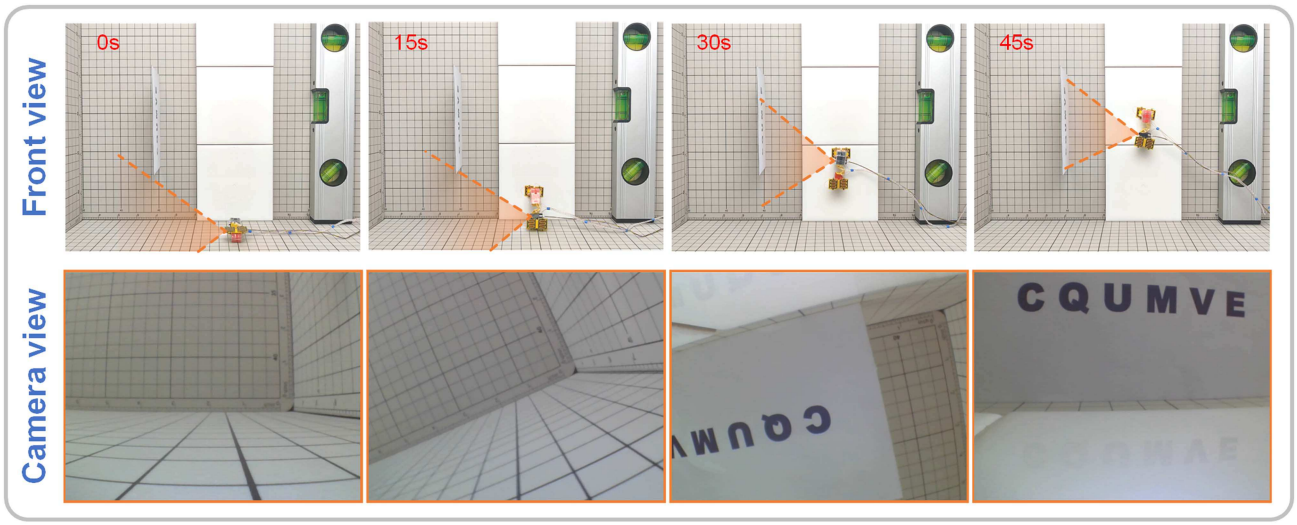

Fig. 15. Demonstration of the robot carrying a miniature camera to climb a vertical wall for inspection. The robot completes a transition motion and then climbs on a vertical wall, capturing the word "CQUMVE" on the card.

to another vertical wall and continued with a turning motion to return to the horizontal wall. The experiment results prove that the robot has an excellent ability to move in a 3-D space.

A sequence of experiments illustrated the robot's climbing ability on different walls. In Fig. 14(c), the robot climbed vertically on a piece of glass, tiles, an aluminum plate, and cardboard. The results demonstrated that the robot could smoothly adsorb and desorb on these materials with the same climbing speed. In addition, the robot can also climb on curved surfaces, which is difficult for most soft climbing robots. As shown in Fig. 14(d), the robot achieved stable climbing on a convex surface with a curvature of $\sim$5.7 m^{-1} and a concave surface with a curvature of $\sim$5.2 m^{-1}, respectively.

Finally, we mounted a miniature camera (1.2 g) on the robot to capture images while in motion, as illustrated in Fig. 15. A card with a width of 120 mm and a height of 70 mm was fixed on the vertical wall. The robot started from the horizontal wall, then transferred to the vertical wall, and performed a linear climbing motion with a horizontal distance of about 90 mm from the card. When the robot climbed to a certain height, the camera fixed on its side captured the word "CQUMVE" printed on the card in its

entirety. This proves that the robot has the ability to carry small equipment such as cameras for transportation, reconnaissance, and detection tasks in unstructured environments.

VI. Conclusion

This article presented a multifunctional soft wall-climbing robot capable of moving, transitioning, and turning over various materials and angles of surfaces. Two models of pneumatic bending actuators were designed, respectively, to enable the robot's moving and turning motions. In addition, a simple open-loop control strategy was proposed based on the theoretical analysis model of the robot. Adaptive EA foot pads were also designed to provide controllable adhesion force on different surfaces, especially curved ones. The overall weight of the soft robot was only 2.57 g by using lightweight materials and structures for the actuators and adhesion units. The experimental results demonstrated that the robot could move at an average speed of 3.85 mm/s (0.08 body length/s) on horizontal, vertical, and inverted walls and make transitions between walls with different pinch angles. It was also illustrated that the robot could turn clockwise at an average speed of 2.23 °/s and counterclockwise at an average speed of 2.97 °/s. Moreover, the robot could also move in multiplanar environments and carried a 1.2 g camera to transition and climb on a vertical wall. Thus, with its unique structure and locomotion, this soft wall-climbing robot has great potential for detection and surveillance in unstructured environments.

Although our robot has demonstrated the ability to move flexibly between multiple walls, many aspects still need further study. For example, adding bending and haptic sensors will provide feedback for the control of the robot and make the robot more intelligent. The robot's structure will be further optimized to reduce the overturning torque during motions and improve locomotion efficiency. In addition, the adhesion units will be theoretically analyzed to select a suitable size and shape to enhance the adhesion force and the load capacity.

References

[1] S. Nansai and R. Mohan, "A survey of wall climbing robots: Recent advances and challenges," *Robotics*, vol. 5, no. 3, Jul. 2016, Art. no. 14.

[2] T. Seo, Y. Jeon, C. Park, and J. Kim, "Survey on glass and façade-cleaning robots: Climbing mechanisms, cleaning methods, and applications," *Int. J. Precis. Eng. Manuf.-Green Technol.*, vol. 6, no. 2, pp. 367–376, Mar. 2019.

[3] S. Chen et al., "Soft crawling robots: Design, actuation, and locomotion," *Adv. Mater. Technol.*, vol. 5, no. 2, Dec. 2020, Art. no. 1900837.

[4] K. Daltorio et al., "Mini-whegs TM climbs steep surfaces using insect-inspired attachment mechanisms," *Int. J. Robot. Res.*, vol. 28, no. 2, pp. 285–302, Feb. 2019.

[5] H. Eto and H. H. Asada, "Development of a wheeled wall-climbing robot with a shape-adaptive magnetic adhesion mechanism," in *Proc. IEEE Int. Conf. Robot. Automat.*, 2020, pp. 9329–9335.

[6] G. Lee et al., "Series of multilinked caterpillar track-type climbing robots," *J. Field Robot.*, vol. 33, no. 6, pp. 737–750, Sep. 2016.

[7] S. de Rivaz et al., "Inverted and vertical climbing of a quadrupedal microrobot using electroadhesion," *Sci. Robot.*, vol. 3, no. 25, Dec. 2018, Art. no. eaau3038.

[8] Y. Liu et al., "Steerable dry-adhesive linkage-type wall-climbing robot," *Mech. Mach. Theory*, vol. 153, Nov. 2020, Art. no. 103987.

[9] S. Mahmood et al., "Propeller-type wall-climbing robots: A review," *IOP Conf. Ser.: Mater. Sci. Eng.*, vol. 1094, no. 1, 2021, Art. no. 012106.

[10] R. Shepherd et al., "Multigait soft robot," *Proc. Nat. Acad. Sci.*, vol. 108, pp. 20400–20403, 2011.

[11] D. Rus and M. Tolley, "Design, fabrication and control of soft robots," *Nature*, vol. 521, no. 7553, pp. 467–475, May 2015.

[12] C. Lee et al., "Soft robot review," *Int. J. Control Automat. Syst.*, vol. 15, no. 1, pp. 3–15, Jan. 2017.

[13] M. Tolley et al., "A resilient, untethered soft robot," *Soft Robot.*, vol. 1, no. 3, pp. 213–223, Sep. 2014.

[14] X. Liu et al., "Worm-inspired soft robots enable adaptable pipeline and tunnel inspection," *Adv. Intell. Syst.*, vol. 4, no. 1, Jan. 2022, Art. no. 2100128.

[15] J. Walker et al., "Soft robotics: A review of recent developments of pneumatic soft actuators," *Actuators*, vol. 9, no. 1, Jan. 2020, Art. no. 3.

[16] S. Li, D. M. Vogt, D. Rus, and R. J. Wood, "Fluid-driven origami-inspired artificial muscles," *Proc. Nat. Acad. Sci.*, vol. 114, pp. 13132–13137, 2017.

[17] Q. Ze et al., "Soft robotic origami crawler," *Sci. Adv.*, vol. 8, no. 13, Mar. 2022, Art. no. eabm7834.

[18] H. Yang, M. Xu, W. Li, and S. Zhang, " Design and implementation of a soft robotic arm driven by SMA coils," *IEEE Trans. Ind. Electron.*, vol. 66, no. 8, pp. 6108–6116, Aug. 2019.

[19] Z. Patterson et al., "A method for 3D printing and rapid prototyping of fieldable untethered soft robots," *Soft Robot.*, vol. 10, pp. 292–300, Apr. 2023, doi: 10.1089/soro.2022.0003.

[20] Q. Wu, V. Pradeep, and X. Liu, "A paper-based wall-climbing robot enabled by electrostatic adhesion," in *Proc. IEEE Int. Conf. Soft Robot.*, 2018, pp. 315–320.

[21] Y. Guo, L. Liu, Y. Liu, and J. Leng, " Review of dielectric elastomer actuators and their applications in soft robots," *Adv. Intell. Syst.*, vol. 3, no. 10, Oct. 2021, Art. no. 2000282.

[22] Y. Liu et al., "Bioinspired triboelectric soft robot driven by mechanical energy," *Adv. Funct. Mater.*, vol. 31, no. 38, Jul. 2021, Art. no. 2104770.

[23] J. Cao, W. Liang, Y. Wang, H. P. Lee, J. Zhu, and Q. Ren, "Control of a soft inchworm robot with environment adaptation," *IEEE Trans. Ind. Electron.*, vol. 67, no. 5, pp. 3809–3818, May 2020.

[24] M. Robertson and J. Paik, "New soft robots really suck: Vacuum-powered systems empower diverse capabilities," *Sci. Robot.*, vol. 2, no. 9, Aug. 2017, Art. no. eaan6357.

[25] Y. Tang, Q. Zhang, G. Lin, and J. Yin, "Switchable adhesion actuator for amphibious climbing soft robot," *Soft Robot.*, vol. 5, no. 5, pp. 592–600, Oct. 2018.

[26] M. A. Graule et al., "Perching and takeoff of a robotic insect on overhangs using switchable electrostatic adhesion," *Science*, vol. 352, no. 6288, pp. 978–982, May 2016.

[27] T. George et al., "Control strategies for soft robotic manipulators: A survey," *Soft Robot.*, vol. 5, no. 2, pp. 149–163, Apr. 2018.

[28] J. Wang and A. Chortos, "Control strategies for soft robot systems," *Adv. Intell. Syst.*, vol. 4, no. 5, May 2022, Art. no. 2100165.

[29] Y. Zhang, D. Yang, P. Yan, P. Zhou, J. Zou, and G. Gu, "Inchworm inspired multimodal soft robots with crawling, climbing, and transitioning locomotion," *IEEE Trans. Robot.*, vol. 38, no. 3, pp. 1806–1819, Jun. 2022.

[30] H. Fu et al., "Interfacing soft and hard: A spring reinforced actuator," *Soft Robot.*, vol. 7, no. 1, pp. 44–58, Feb. 2020.

[31] W. Yu et al., "A minimally-designed soft crawling robot for robust locomotion in unstructured pipes," *Bioinspiration Biomimetics*, vol. 17, no. 5, Jul. 2022, Art. no. 056001.

[32] G. Gu, J. Zou, R. Zhao, X. Zhao, and X. Zhu, "Soft wall-climbing robots," *Sci. Robot.*, vol. 3, no. 25, Dec. 2018, Art. no. eaat2874.

[33] L. Qin et al., "A versatile soft crawling robot with rapid locomotion," *Soft Robot.*, vol. 6, no. 4, pp. 455–467, Aug. 2019.

[34] B. Liao et al., "Soft rod-climbing robot inspired by winding locomotion of snake," *Soft Robot.*, vol. 7, no. 4, pp. 500–511, Aug. 2020.

[35] Y. Guo, J. Guo, L. Liu, Y. Liu, and J. Leng, "Bioinspired multimodal soft robot driven by a single dielectric elastomer actuator and two flexible electroadhesive feet," *Extreme Mech. Lett.*, vol. 53, May 2022, Art. no. 101720.

[36] W. Pang et al., "A soft microrobot with highly deformable 3D actuators for climbing and transitioning complex surfaces," *Proc. Nat. Acad. Sci.*, vol. 119, 2022, Art. no. e2215028119.

[37] M. S. Verma, A. Ainla, D. Yang, and D. Harburg, "A soft tube-climbing robot," *Soft Robot.*, vol. 5, no. 2, pp. 133–137, Apr. 2018.

[38] C. Cao et al., "Theoretical model and design of electroadhesive pad with interdigitated electrodes," *Mater. Des.*, vol. 89, no. 5, pp. 485–491, Jan. 2016.

[39] K. H. Koh, M. Sreekumar, and S. G. Ponnambalam, "Hybrid electrostatic and elastomer adhesion mechanism for wall climbing robot," *Mechatron.*, vol. 35, pp. 122–135, May 2016.

Rui Chen (Member, IEEE) received the B.S. and Ph.D. degrees in mechanical engineering from the Beihang University, Beijing, China, in 2009 and 2014, respectively.

He is currently a Professor with the College of Mechanical and Vehicle Engineering, Chongqing University, Chongqing, China. His research interests include soft robots and bioinspired robots.

Xinrui Tao received the B.S. degree in mechanical engineering from the Xiangtan University, Xiangtan, China, in 2020. He is currently working toward the M.S. degree in mechanical engineering with the Chongqing University, Chongqing, China.

His research interests include soft robotics and electroadhesion.

Changyong (Chase) Cao (Member, IEEE) received the Ph.D. degree in mechanical engineering and materials science from the Australian National University, Canberra, ACT, Australia, in 2014.

He completed his postdoctoral training in mechanical engineering and electrical engineering with the Duke University, Durham, NC, USA, in 2017. He is currently an Assistant Professor in Mechanical and Aerospace Engineering with the Case Western Reserve University, Cleveland, OH, USA. He is also an Investigator of the Advanced Platform Technology Center, Louis Stokes Cleveland VA Medical Center, Cleveland, OH, USA. His research interests include soft (active) materials, soft robotics, self-powered electronic systems, and 3-D/4-D printing of multifunctional materials.

Pei Jiang (Member, IEEE) received the B.S. and Ph.D. degrees in control science and engineering from the Zhejiang University, Hangzhou, China, in 2008 and 2015, respectively.

He is currently an Associate Professor with the College of Mechanical and Vehicle Engineering, Chongqing University, Chongqing, China. His research interests include robotic systems, soft robotics, and energy modeling of industrial robots.

Jun Luo received the B.S. and M.S. degrees in mechanical engineering from the Henan Polytechnic University, Jiaozuo, China, in 1994 and 1997, respectively, and the Ph.D. degree in mechanical engineering from the Research Institute of Robotics, Shanghai Jiao Tong University, Shanghai, China, in 2000.

He is currently a Professor with the State Key Laboratory of Mechanical Transmissions, Chongqing University, Chongqing, China. His research interests include robot sensing, human–machine interfaces, and special robotics.

Yu Sun (Fellow, IEEE) received the B.S. degree in electrical engineering from the Dalian University of Technology, Dalian, China, in 1996, the M.S. degree from the Institute of Automation, Chinese Academy of Sciences, Beijing, China, in 1999, and the Ph.D. degree in mechanical engineering from the University of Minnesota, Minneapolis, MN, USA, in 2003, respectively. He is currently a Professor with the University of Toronto (UofT) and Director of the UofT Robotics Institute. His lab specializes in developing innovative technologies and instruments for manipulating and characterizing cells, molecules, and nanomaterials.

Prof. Sun is a Fellow of Canadian Academy of Engineering, a Fellow of The Academy of Science of Royal Society of Canada, and a Foreign Member of Chinese Academy of Engineering. He was also elected Fellow of IEEE, ASME, AIMBE, AAAS, NAI, CSME, and EIC for his work on micro–nano devices and robotic systems.